Faraday Discussions

Cite this: DOI: 10.1039/d5fd00157a

PAPER

Modulating multivalent ion interaction in angstrom-scale confinement through solvent environment

Xiaolin Yue, [a] Mingzhan Wang, [ab] Dongchen Ying [a] and Chong Liu *[a]

Received 8th December 2025, Accepted 14th January 2026
DOI: 10.1039/d5fd00157a

When the size of the confinement approaches that of individual molecules and ions at the angstrom-scale (Å-scale), intriguing ion–ion and water–ion interactions emerge. Water, being a unique solvent, has asymmetric dielectric constants and discrete configurations within Å-scale confinement. However, how these distinctive characteristics of water affect ion behaviors as well as how they translate to other solvents remains largely unexplored. Here, with the robust platform of functionalized two-dimensional molybdenum disulfide nanochannels, we systematically probed how the solvent environment regulates ion dynamics, uptake, and selectivity in Å-scale confinement, using rare-earth elements (REEs) as a model system due to their periodic properties and practical relevance. By tuning solvent composition, we find that both ion uptake and selectivity are governed by the interplay between binding-site deprotonation controlled by solvent-dependent acidity and dielectric effects mediated by the solvent environment. Maximum uptake was observed at intermediate solvent ratios where acidity and dielectric properties are balanced. Increasing deprotonation in dimethylformamide-rich systems shifts selectivity toward heavier REEs. Dynamic tests further reveal that the preference for heavy element Yb arises from stronger binding and improved channel accessibility, facilitated by carboxylate formation and lighter-element-assisted channel opening. Collectively, these findings highlight solvent composition as a powerful lever for tuning ion behavior in 2D channels, and provide mechanistic insight into solvent-mediated approaches to selective REE recovery and separation.

Introduction

Nanofluidics, with confinement at the nanometer length scale and below, gives rise to unique transport behaviors of water and ions. The advances in

[a]Pritzker School of Molecular Engineering, University of Chicago, Chicago, IL 60637, USA. E-mail: chongliu@uchicago.edu
[b]Department of Materials Science and Engineering, City University of Hong Kong, Hong Kong SAR 999077, China

nanofabrication enable material structures and channel dimensions to be controlled precisely.[1–4] When the confinement size approaches that of individual ions or molecules at the angstrom scale (Å-scale), the continuum description of fluids breaks down, giving way to more pronounced finite-size and interfacial effects.[5] As a result, fluidic behavior deviates from that in the bulk, giving rise to unique confinement-induced phenomena. Water is the most widely used solvent due to its abundance and distinctive physicochemical properties. Under extreme confinement, water molecules reorganize into well-defined, discrete layers.[6–9] This structural ordering gives rise to highly anisotropic physical properties. In particular, the dielectric response becomes asymmetric, exhibiting an anomalously low out-of-plane dielectric constant and an exceptionally large in-plane value on the order of 10^3.[10,11] Such discrete configurations and dielectric anisotropy significantly reshapes the electrostatic landscape within nanoconfined channels, facilitating interactions such as dielectric exclusion and long-range ion–ion correlations. Consequently, anomalous ion behaviors emerge under Å-scale confinement, including correlated ion motion[12,13] and anomalously enhanced transport.[14,15]

However, the translation of confinement phenomena from water to other solvents remains largely unexplored. The solvent effect was investigated mostly in bulk systems, particularly in the context of battery electrolytes.[16,17] Solvent size and solvation energy govern the Li^+ transport mechanism in electrolytes. Large solvent molecules form bulky solvation shells that slow Li^+ conduction through vehicular or structural mechanism depending on salt concentration,[18] whereas small, weakly bound solvents enable ultrafast conduction through a novel ligand-channel transport pathway.[19] Beyond these structural factors, solvent polarizability and proticity could also modulate ion–solvent interactions and thereby affect ion dynamics.[20] Protic solvents stabilize ions through hydrogen bond and ordered solvation shells, whereas aprotic solvents exhibit a less structured local environment dominated by dipolar interactions.[21] Hence, ion diffusion is influenced by the altered ion stability and pairing: strongly hydrogen-bonding solvents slow ion mobility due to structured solvation, while solvents with suitable polarizability enhance electric-field driven charge transport by reducing ion pairing. Under Å-scale confinement, these solvent-dependent effects could become more pronounced, as the limited spatial dimension induces partial desolvation and further restructures the solvation shell.

In two-dimensional (2D) nanochannels, the relatively less rigid confinement compared to one-dimensional nanopores allows solvent molecules and ions to experience strong yet flexible interactions with the channel environment. The confined space distorts or partially strips the ion hydration or solvation shells, particularly for ions with large shells.[22] Interactions between solvent molecules and channel walls become dominant under Å-scale confinement, leading to remarkably high solvent fluxes governed by confinement-determined fluid parameters such as average density, viscosity, and slip length.[23] These properties are further tunable through surface chemistry engineering of the channel walls,[24] where hydrophilicity or hydrophobicity modulates interfacial friction and transport behavior. Swelling or solvent uptake in lamellar 2D materials could also induce fluctuations in the interlayer spacing, thus altering effective channel size and modulating semi-permeability.[25] The altered solvent behavior under confinement, in turn, affects ion structure and interactions with the channel. The

dielectric properties of confined solvent play a particularly critical role. When ions enter a medium with different dielectric constant—such as a membrane matrix relative to the surrounding solvent—they interact with the polarized interface and experience image forces that give rise to dielectric exclusion,[26] which increases the energy barrier for ion permeation and selectively hinders the partitioning of strongly solvated ions.[27] These solvent-mediated and dielectric effects shape ion selectivity and mobility *via* ion-specific factors such as solvation shell stability and desolvation energy. Despite extensive studies on 2D channels under aqueous conditions, investigations into solvent effects to modulate confined ion dynamics are few. Understanding these effects could uncover new transport mechanisms and enable the rational design of effective ion conduction and separation systems, especially for applications of emerging technological importance, such as rare earth element (REE) separation.[28]

In this study, we systematically investigate ion dynamics, uptake, and selectivity in both water and a representative organic solvent within Å-scale 2D channels built from acetic acid functionalized molybdenum disulfide (MoS_2-COOH). *N*,*N*-Dimethylformamide (DMF) was identified as a solvent candidate for its strong solvating ability, low viscosity, and excellent miscibility with water. Although DMF has a lower dielectric constant than water, it remains relatively high among organic solvents. This intermediate dielectric environment balances electrostatic screening and specific solvation, providing a tunable platform to modulate ion–solvent and ion–ion interactions, and thereby making DMF an ideal medium for probing solvent effects on ion behaviors in confinement. For model ion system, REEs were selected due to their periodic variation in Lewis acidity as well as their practical importance. Trivalent REE cations were chosen as the predominant existing form in solution. By varying the ratio between water and DMF, we uncovered how key solvent properties, such as dielectric constant, acidity, and solvating ability, govern ion dynamics and selective uptake in confined 2D channels. Our results show that ion uptake and selectivity are governed by the balance between binding-site deprotonation controlled by solvent-dependent acidity and dielectric effects mediated by the solvent environment. Uptake is maximized at intermediate solvent compositions, where moderate acidity and dielectric constant support both deprotonation of carboxylate sites and favorable ion stabilization. As the solvent becomes DMF-rich, increased deprotonation enhances binding strength and shifts selectivity toward heavier REEs. Time-dependent uptake tests further reveal that heavy element Yb is taken up more readily in REE mixtures due to its stronger binding and improved access into the channel, a process aided by carboxylate formation and channel opening assisted by lighter elements. Overall, our work demonstrates that the ion dynamics, uptake, and selectivity in confined channels can be controlled *via* bulk physical properties of the solvent and its composition, offering insight into solvent-mediated ion transport and enabling design of solvent-engineered membranes for targeted REE recovery and separation.

Solvent effect on channel structure

Å-Scale confinement is built by restacking MoS_2-COOH nanosheets into membranes, where acetate functional groups act as both spacers between layers as well as binding sites for metal cations.[14] To quantitatively examine the layered

structure of the membrane in solution, the structures of the 2D channels with REE ions inside were characterized by X-ray diffraction (XRD), where the measured interlayer spacing corresponds to the channel height. From the XRD spectra (Fig. 1A), the MoS_2-COOH channel in pure water under wet state is 10.8 Å. The effective confinement dimension, or free spacing, of the 2D channel can be obtained by subtracting the intrinsic thickness of a monolayer MoS_2 nanosheet (~6.2 Å) from the measured interlayer spacing. This calculation yields a free spacing of approximately 4.6 Å, which points to a bilayer-water structure confined within the channel. When water is the sole solvent, the (002) and (004) peaks shift to higher angles after REE ion uptake. As the atomic number increases in the lanthanides, the interlayer spacing gradually decreases from 13.2 Å (free spacing 7.0 Å) to 12.3 Å (free spacing 6.1 Å) (Fig. 1C). This is the opposite of the increasing trend in hydration radius from light to heavy elements, and it denotes that the

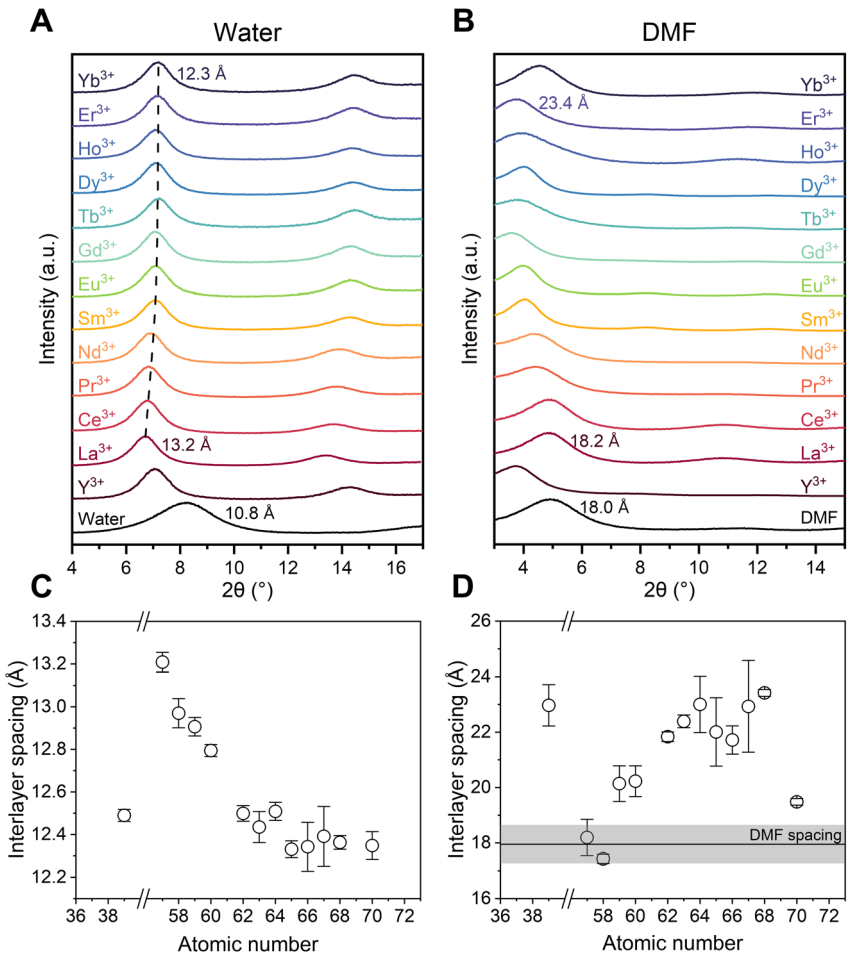

Fig. 1 Structures of 2D channels with REE ion uptake. (A and B) XRD spectra of MoS_2-COOH membranes with individual REE ion in water and DMF. (C and D) Corresponding interlayer spacing in water and DMF.

electrostatic interactions between the REE ions and the negatively charged channel wall with $-COO^-$ groups are so strong that the layers are pulled closer together as the Lewis acidity of the ions increase.

In sharp contrast, the DMF system exhibits significantly larger interlayer spacing, reaching around 18.0 Å (free spacing 11.8 Å) in the wet state and expanding further in the presence of ions (Fig. 1B). Heavier REE tend to have larger interlayer spacings than lighter ones but the trend is not monotonic (ranging from 18.2 Å for La^{3+} to 23.4 Å for Er^{3+}, with outliers 17.4 Å for Ce^{3+}, 22.0 Å for Tb^{3+}, 21.7 Å for Dy^{3+}, 22.9 Å for Ho^{3+}, and 19.5 Å for Yb^{3+}) (Fig. 1D), which could be related to both the configurations of molecules in the channel and ion uptake amount such as in the case for Yb^{3+}. Yb^{3+} shows a smaller spacing, likely due to its relatively low uptake (Fig. S1). Light REE cations, in particular La^{3+} and Ce^{3+}, exhibit slightly larger interlayer spacing compared with neat DMF with no ions, suggesting that their influence on the channel structure is minimal. This is consistent with the lower uptake of light REE cation, which is related to their lower Lewis acidity and therefore weaker interaction with the acetate functional group. Heavy REE cations interact more strongly with the acetate group which leads to larger amounts of uptake. In particular, the interlayer spacing exceeds 20 Å for heavy elements, such as 23.4 Å (free spacing 17.2 Å) for Er^{3+}. The interlayer spacing is crucial in determining the desolvation and ion coordination configuration which affect the REE selectivity. Therefore, we examine the ion uptake preferences in mixed REE systems to investigate the complex interplay between ions, solvent, and the channel.

Solvent effect on ion uptake and selectivity

To examine the effect of DMF fraction on ion behavior, different DMF–water compositions were investigated for uptake using 13 REE mixture solutions. The interlayer spacing and ion uptake amount of MoS_2-COOH membrane were measured (Fig. 2A). Solutions containing 13 REE cations (Y^{3+}, La^{3+}, Ce^{3+}, Pr^{3+}, Nd^{3+}, Sm^{3+}, Eu^{3+}, Gd^{3+}, Tb^{3+}, Dy^{3+}, Ho^{3+}, Er^{3+}, Yb^{3+}) were prepared at varying DMF–water molar ratios, ranging from 0 (pure water) to 35 : 1, with 35 : 1 representing hydrated REE salts in neat DMF solvent. As DMF fraction x_{DMF} increases, the interlayer spacing of the membrane did not change much until x_{DMF} reaches 0.25. After that the interlayer spacing increases with increasing x_{DMF}, and a relatively large spacing was observed at equal molar composition of DMF and water, marking the transition point at which bulky DMF molecules dominate the channels and lead to a more pronounced swelling. At the highest DMF fraction $x_{DMF} = 0.97$, the interlayer spacing expands to over 22 Å, which is in agreement with the spacing observed for individual heavy REE in DMF solutions. Complementary attenuated total reflectance Fourier transform infrared (ATR-FTIR) measurements on wet membranes (Fig. S13) show that the evolution of the DMF carbonyl vibrational features reflects a composition-dependent change in the confined solvent environment. In particular, the spectra reveal a transition from water-like, strongly hydrogen-bonded DMF at low x_{DMF} to more weakly coordinated DMF at high x_{DMF}, consistent with the observed swelling behavior and changes in ion uptake.

The species and amounts of the uptake ions were measured using inductively coupled plasma mass spectrometry (ICP-MS). The total amount of REE uptake

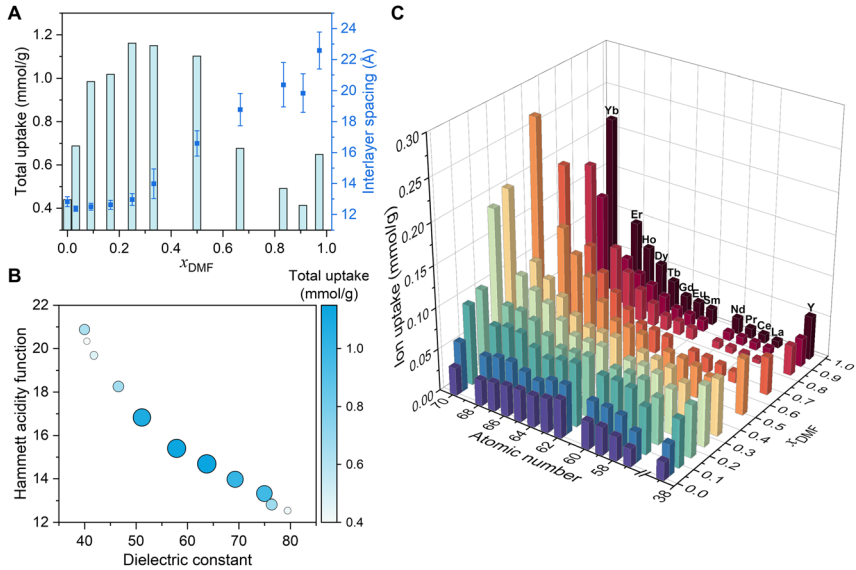

Fig. 2 Ion uptake behavior of 2D channels in DMF–water media. (A) Total ion uptake and corresponding interlayer spacing as a function of DMF fraction x_{DMF} (from left to right, DMF–water molar ratios are 0, 1 : 30, 1 : 10, 1 : 5, 1 : 3, 1 : 2, 1 : 1, 2 : 1, 5 : 1, 10 : 1, and 35 : 1). (B) Bubble plot showing the three-dimensional correlation of dielectric constant, Hammett acidity function and total uptake. Dielectric constant and acidity function values for DMF–water mixtures are taken from literature and summarized in Table S1. (C) Ion uptake of individual REE ion *versus* DMF–water ratio, showing preferential uptake for heavy elements with higher DMF fraction.

shows a nonmonotonic, volcano-shaped dependence on the DMF fraction, as it rises from pure water composition, reaches a maximum near x_{DMF} of 0.25–0.33, and subsequently decreases with further increases in DMF content. When x_{DMF} reaches the pure-DMF composition ($x_{DMF} = 0.97$), a slight rebound in the total ion uptake is observed, which could be due to the presence of unique solvent–solute interactions in the nearly water-free regime. DMF is a highly polar solvent molecule, with an electronegative carbonyl oxygen and electron-donating methyl groups. In DMF-rich ionic solutions, cations are preferentially solvated through coordination with the strongly negative oxygen ends, whereas anions are destabilized, because the methyl groups restrict access to the positive end of the dipole.[29,30] The high polarity of DMF gives rise to the unique bulk physicochemical properties of the DMF environment, in particular their acidity and dielectric constant, while the asymmetric solvation of cations and anions could further alter solvent–ion interactions in DMF solutions.

The dielectric constant reflects a solvent's ability to screen electrostatic forces between charged species. Solvents with a high dielectric constant effectively reduce coulombic interactions, thus stabilizing ions and charges. On the other hand, acidity, which is usually expressed through proton activity or practical pH, governs the protonation state and accessibility of acetate functional groups as binding sites. A less acidic environment facilitates the deprotonation of carboxylic acid groups (–COOH/–COO^-), thereby enhancing coordination with the cationic

species. Water has a much higher dielectric constant (79.5) than DMF (39.9);[31] however, DMF exhibits a higher practical pH because of its basicity and wider length of pH scale (18.0 units).[32] Therefore, as the DMF fraction increases in the ion mixture solution, the dielectric constant of the mixture decreases, while practical pH increases. These two factors induce opposing effects that jointly regulate the total amount of ion uptake: a lower dielectric constant destabilizes ionic species in the channel due to weaker screening between charges and decreases ion uptake, whereas a higher pH leads to deprotonation of functional groups and increases the number of available binding sites. Together, these effects establish an optimal DMF–water composition that maximizes ion uptake.

To provide a qualitative understanding of this relationship, experimental values of the dielectric constant and Hammett acidity function (H_0) for DMF–water mixtures were obtained from literature and summarized in Table S1. The experimental dielectric constant of aqueous DMF was extracted from dielectric relaxation studies using time-domain reflectometry, a technique that measures dielectric response over a broad frequency range (10 MHz to 10 GHz) and allows accurate characterization of static and frequency-dependent dielectric properties in pure and mixed solvents.[31] The Hammett acidity function quantifies a medium's ability to remove proton from a neutral, weakly acidic substrate AH, and is widely used in non-aqueous systems to characterize practical pH.[33] For DMF–water mixtures, the H_0 was determined by measuring the protonation ratios of weakly acidic indicators in the presence of base (0.019 M tetramethylammonium hydroxide) and calculating values using the Hammett relation.[34] Although temperature affects the absolute values of these solvent parameters, their relative ordering remains unchanged across DMF–water compositions. Both Hammett acidity function and dielectric constant were plotted alongside the total ion uptake in a bubble plot (Fig. 2B), illustrating the correlation between bulk solvent properties and ion uptake behavior. The results highlight a balance between two competing solvent-dependent effects, and the maximum of ion uptake amount occurs only at moderate dielectric constant and acidity. At a relatively low acidity, which corresponds to a higher practical pH, protons are stripped from acetate groups, thereby exposing negatively charged sites available for cation coordination. However, the coordination of the trivalent REE ion with deprotonated carboxylate groups ($-COO^-$), constrained by the limited density of functional groups, generates excess positive charge that needs to be stabilized by the surrounding medium. A moderately high dielectric constant environment provides this stabilization by screening electrostatic repulsions between these charged species, allowing for higher local ion densities. Overall, these results suggest that the DMF system exhibits a unique balance between binding site availability and solvent-mediated electrostatic effects, with ion uptake in MoS_2-COOH channels peaking at intermediate DMF–water compositions where both dielectric properties and acidity fall within moderate values. It should be noted, though, that the local pH and dielectric environment within the confined channel is unknown and would require more advanced characterization to fully understand their influence on ion uptake. Nevertheless, even in the absence of direct measurements, confinement is expected to induce solvent orientation preference and interfacial ordering in polar solvents, reducing the effective local dielectric response.[35] At high DMF fractions, DMF molecules could be preferentially adsorbed onto the MoS_2 surfaces due to their high dipole

moment, forming an ordered interfacial layer. The interlayer spacing under DMF-rich conditions is sufficiently large to accommodate this structural ordering, leading to a reduced effective dielectric constant within the channel. While a lower dielectric constant can enhance electrostatic interactions near the channel walls, it also raises the energetic penalty for ions to enter the channel from bulk solution or reside in the channel especially in the center, where dielectric stabilization is reduced. This unfavorable energetic landscape can limit ion accessibility, ultimately lowering overall ion uptake at high DMF content. In contrast, at intermediate DMF fractions, a balance between interfacial solvent ordering and dielectric stabilization is achieved, creating an optimal confinement environment for maximal ion uptake.

The solvent content not only controls the total ion uptake, but also shapes the ion uptake preferences in mixed REE systems. The uptake amount of each individual ion in the 13 REEs mixture is shown in Fig. 2C, and a distinct shift in element preference is revealed. In pure water solution ($x_{DMF} = 0$), the uptake trend of mixed REEs exhibits a volcano shape peaked at Sm^{3+}. This results from a trade-off between dehydration penalties, channel binding, and uptake kinetics. From light to heavy REEs, Lewis acidity of the ion increases, leading to stronger solvation by the solvent molecules. The dehydration barrier for heavy REEs such as Dy^{3+} is much larger than a light REE such as La^{3+} and a transition one such as Sm^{3+}.[36] Consequently, REEs with intermediate Lewis acidity, such as Sm^{3+}, achieve the highest uptake in the mixture. This is owing to the fast kinetics of Sm^{3+} to enter the channel and modulate the channel spacing to increase the entry barrier for others as well as its strong binding strength which makes ion replacement difficult in the channel.

As DMF fraction x_{DMF} increases, heavy elements gradually become favored, and in solutions with moderate-to-high DMF content ($x_{DMF} > 0.50$), the overall uptake trend for the 13-mixture transitions to a monotonic increase with selectivity toward the heavier elements. This trend at high x_{DMF} is similar to that with increasing pH.[36] Increasing DMF fraction enhances deprotonation of carboxylate groups on the channel wall, although excessively high DMF content would reduce the total amount of ion uptake, as discussed above. This indicates that, in DMF-rich environments, when carboxylate sites are deprotonated, the binding favors heavy elements and the binding energy is sufficiently strong to compensate for the desolvation penalty. The selectivity transition to Yb^{3+} is obvious at x_{DMF} of 0.25. For $x_{DMF} = 0.25$, the interlayer spacing is still dominated by water at a narrow spacing; however, the uptake is among the highest. This also points to the deprotonation of the carboxylic acid group being critical for the observed selectivity trend instead of the dehydration barrier.

To further compare between the solvent effect and pH effect, the mixed REEs uptake was carried out in DMF–water mixtures both before and after pH adjustment with potassium hydroxide (KOH). Upon increasing the pH to ~6.5, the uptake curves at different DMF–water ratio all converge into a monotonic increasing trend (Fig. S3), indicating that higher pH enhances selectivity to heavy REE. Nevertheless, while total uptake amounts are comparable in $x_{DMF} = 0.97$ without pH adjustment and water adjusted to pH of 6.5, the DMF system exhibits markedly better selectivity for heavy over light elements, suggesting that beyond pH-induced effects, solvent–ion interactions intrinsic to DMF also play a crucial role in enhancing heavy-element selectivity.

Solvent effect on ion dynamics and selectivity

To gain deeper insight into the mechanisms underlying ion selectivity, we investigate how the selectivity between heavy and light elements evolves under dynamic processes. Time-dependent uptake profiles in DMF (Fig. 3A) show that even at the very beginning of the uptake process, the preference is for heavier elements, particularly Yb. However, the overall low uptake amount during the early stages indicates sluggish kinetics in DMF. This could be attributed to the high energy barrier required to expand the channels (overcoming material strain) to the favorable interlayer spacing necessary to accommodate both the REE ions and bulky solvent molecules. Nevertheless, there are two types of expansion. One is from solvent entering the channel (8.2 Å expansion) and the other one from REE ions entering the channel (additional 4.6 Å expansion). The barrier for solvent entrance can be lowered by introducing a pre-soak step, during which the membrane is left to swell in the corresponding solvent prior to ion uptake. This process expands the channels and facilitates the entry of large REE ions. As shown by the time-dependent ion uptake in DMF with and without pre-soaking (Fig. 3A and S6A), this pretreatment step accelerates the uptake process while maintaining the same ion preference during dynamic uptake, increasing the Yb uptake rate by approximately 1.6-fold for the first 30 min. However, the slow uptake is not fully resolved after pre-soaking, which points to ion entrance related channel expansion having a stronger influence on the dynamics. For comparison, similar time-dependent uptake tests were performed in water with and without the pre-soak step. The results (Fig. S6B and S7A) show that ion dynamics are substantially faster in aqueous conditions compared with that in DMF. No discernible difference was observed between those with and without pre-soak over the duration tested. This contrast highlights the profound influence of solvent properties on ion uptake kinetics. All subsequent experiments were performed using dry membranes without a pre-soak step unless otherwise noted. This approach ensures consistent initial conditions across all systems and allows the intrinsic solvent dynamics to be included in the analysis.

Channel expansion is also important in determining ion interplay during competitive uptake. To further elucidate the temporal evolution of selectivity and the underlying ion dynamics that govern ion preference, we examined three

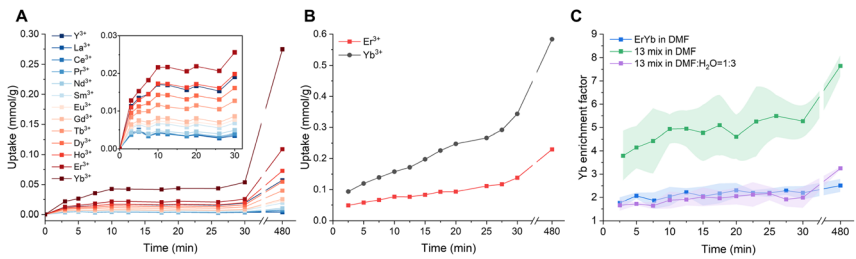

Fig. 3 Dynamics of REE ion uptake and selectivity. (A) Time-dependent uptake of 13 REE mixture in DMF. Inset: expanded view of the initial 30 min of uptake. (B) Time-dependent uptake of Er and Yb binary mixture in DMF. (C) Dynamics of Yb selectivity quantified by Yb enrichment factor.

systems in DMF: a full mixture of all 13 REEs (Fig. 3A), a binary mixture of heavy elements Er and Yb (Fig. 3B), and a single ion solution of Yb (Fig. S8). The total ion concentration was kept comparable to ensure consistent osmotic pressure as the driving force. Since the total amount of ion uptake differs among the three cases (Fig. S9A), the total uptake dynamics were also plotted by normalizing to their final values (Fig. S9B). In the single-Yb case, the uptake proceeds rapidly at the beginning (<10 min), with higher normalized uptake than in both the binary and 13 REE mixture, but then slows down. Although Yb^{3+} uptake amount continues to increase, there is obviously a kinetic barrier that makes Yb^{3+} uptake slow, and with Yb^{3+} alone, the uptake can only proceed to a certain extent with much lower total uptake amount. The limited interlayer spacing expansion is correlated to the low Yb^{3+} uptake. The interlayer spacing only expands to 19.5 Å with Yb^{3+} alone (Fig. 1D), compared with 22.6 Å (Fig. 2A) in the case of the 13 REE mixture. The uptake kinetics are the fastest for the binary mixture of Er and Yb. This result points to the importance of the presence of other lighter elements (even only Er) in further expanding the interlayer spacing and increasing Yb uptake. In the case of the binary Er–Yb mixture, channel opening and Yb^{3+} entrance facilitated by Er^{3+} both occur on a much faster timescale than the time duration of the overall uptake experiment. Therefore, as seen from the Yb/Er ratio (Fig. S10A), the selectivity remains largely unchanged with only a slight increase over time, which reflects their intrinsic entrance selectivity induced by the deprotonated carboxylate acid groups. The Yb enrichment factor was also calculated for the 13 REE mixture, defined as the ratio of Yb to all other REEs in the membrane, normalized by their corresponding ratio in the feed solution. The detailed definition is provided in the SI. As shown in Fig. 3C, the Yb enrichment factor is higher in the presence of light REEs compared to that in the binary Er–Yb case, which can be understood by the higher Yb selectivity over other lighter elements. Notably, in the case of the 13 REE mixture in DMF, the enrichment factor for Yb increases noticeably throughout the uptake process. This could be due to the fact that the layer expanding capability of some lighter REEs could be stronger than Er^{3+}. Therefore, we analyzed the change of Yb/Ln ratio (where Ln denotes all other REEs except Yb) with respect to time (Fig. S10B). The Yb/Ln ratio for Er, Ho, and Dy are relatively similar from the beginning to the end within ~2-fold of change. Therefore, selectivity could reflect their entrance preference which is similar to the case of the binary Er–Yb mixture. For all other elements, there is a significant increase in Yb/Ln ratio over time. However, there could be two reasons behind this. On the one hand, it could be that the other REEs have stronger channel opening capability that they enter the channels first. As the interlayers are expanded, Yb^{3+} would quickly catch up and dominate the uptake due to its fast entry, therefore resulting in Yb/Ln ratio increase over time. On the other hand, the increasing Yb/Ln ratio could come from a saturated uptake of other REEs when the ion preference is low. As shown in the inset of Fig. 3A, the uptake of La^{3+}, Ce^{3+}, Pr^{3+}, and Nd^{3+} saturated after 5 min. Therefore, they belong to the second case. Based on uptake dynamics, Sm^{3+}, Eu^{3+}, and Gd^{3+} could be the ones that have stronger capability in channel expansion which correlates with their wider interlayer spacing in their single ion uptake cases (Fig. 1C and D). Overall, Yb^{3+} alone shows much lower uptake during both dynamic uptake (Fig. S8) and at equilibrium (Fig. S1), with a relatively narrow equilibrium interlayer spacing (Fig. 1D). Yb^{3+} alone cannot efficiently expand the channel, and yet this expansion

process is the bottleneck step for its uptake. In contrast, some lighter REEs in the bulk can assist in expanding the channel, thus lowering the energy barrier for Yb entrance.

Together, the dynamic uptake results reveal the key factors that led to the heavy REE selectivity in DMF dominated solutions. Ion entrance into the confined 2D channel is a critical step in determining its selectivity. In REE mixtures, lighter REEs can facilitate the channel opening to different degrees, and the deprotonated carboxylic acid enables fast entry of Yb^{3+} from the mixture. After Yb^{3+} has already bound to the acetate functional groups, replacement by other REE ions is unlikely. Therefore Yb^{3+} has a much higher selectivity compared with all other REE. Without DMF, the carboxylic acid groups are mostly protonated. In this case, Sm^{3+} enters the channel the fastest and maintains its selectivity throughout the entire uptake process, further supporting ion entry as the critical step in determining selectivity.[36] However, the preferred entering species differs by chemical environment: Yb^{3+} is favored when acetate groups are deprotonated and negatively charged, whereas Sm^{3+} is favored when acetic acid groups are protonated and neutral.

Building on this understanding, we examined another time-dependent uptake in a DMF–water mixture at x_{DMF} of 0.25. At $x_{DMF} = 0.25$, the system exhibited a large total ion uptake despite a relatively small and unexpanded interlayer spacing at equilibrium (Fig. 2A). The results (Fig. S7B) show faster dynamics and high overall uptake, consistent with the observed equilibrium behavior. The Yb enrichment factor in the aqueous mixture ($x_{DMF} = 0.25$) was significantly lower than in DMF-rich solution ($x_{DMF} = 0.97$) with the same REE composition, which shows a slight increase over time (Fig. 3C). This is related to a lower degree of deprotonation at $x_{DMF} = 0.25$ compared to at $x_{DMF} = 0.97$ (Fig. 2B). Moreover, the relatively narrow interlayer spacing at $x_{DMF} = 0.25$ and fast kinetics in the presence of water decrease heavy REEs promotion facilitated by light REEs.

Since interlayer spacing is important in determining the ion interplay in channel opening, the Yb selectivity in the 13 REE mixture was measured and calculated under various solvent environments (Fig. 4A). Across these solvent conditions, the relationship between uptake selectivity and interlayer spacing still

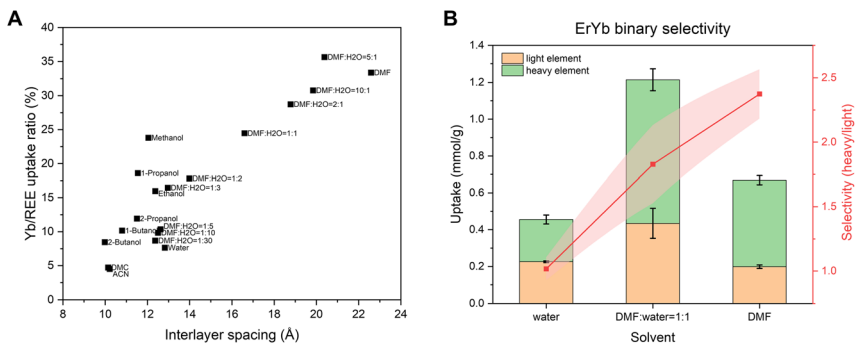

Fig. 4 Solvent-dependent Yb selectivity in 2D channels. (A) Correlation between Yb selectivity and membrane interlayer spacing in the 13 REE mixture, highlighting enhanced Yb/total REE uptake with larger spacing. (B) Yb/Er selectivity in binary mixtures with varying DMF content, showing greater Yb preference at higher DMF levels.

holds. Notably, a clear trend emerges: larger interlayer spacing leads to higher selectivity for heavy element Yb over all other REEs. Among the solvents tested, DMF systems exhibit the highest Yb selectivity. Leveraging this effect, DMF is used to enhance binary selectivity for heavy REEs. For instance, Er and Yb uptake show no significant difference in pure water; however, in the presence of DMF, the selectivity of Yb over Er is substantially increased, reaching a binary selectivity of 1.8 at $x_{DMF} = 0.5$ with an enhanced uptake capacity and a binary selectivity of 2.4 at $x_{DMF} = 0.97$. This enhancement also extends to heavy/light and heavy/intermediate REE pairs, as demonstrated in La–Yb and Sm–Yb binary mixtures (Fig. S11), both of which show pronounced improvements in selectivity at $x_{DMF} = 0.97$ from 1.4 to 30.7, and from 0.6 to 8.9, respectively. Overall, these results highlight the critical role of solvent choice in governing the spacing and chemistry of the confined 2D channel, thereby tuning the selective uptake of REEs.

Conclusions

In summary, we systematically studied the effect of solvent environment on ion dynamics, uptake, and selectivity in Å-scale 2D MoS_2-COOH channels, with a particular focus on nonaqueous organic solvent DMF. By varying solvent composition, we demonstrate that the interplay of dielectric screening and acidity governs both the uptake capacity and selective enrichment of REEs within the channels. Water systems exhibit fast dynamics and a preference for intermediate REEs. In DMF systems, heavy REEs such as Yb dominate the channels due to stronger binding and entrance favorability facilitated by deprotonated carboxylic acid groups and lighter REEs for channel opening. Mixed DMF–water systems exhibit a volcano-shaped uptake dependence on solvent composition, reflecting the competing effects of dielectric stabilization and deprotonation of binding sites. Furthermore, interlayer spacing correlates with selectivity, where the larger spacings present in DMF-rich environments are accompanied by preference for heavy REE like Yb. Overall, these findings establish solvent composition as a powerful tool to modulate ion selectivity and uptake under confinement, offering new pathways for solvent-engineered membranes in selective REE recovery, purification, and advanced ion separation technologies.

Methods

Preparation of ion solutions

REE hydrated nitrate salts $Y(NO_3)_3 \cdot 6H_2O$, $La(NO_3)_3 \cdot 6H_2O$, $Ce(NO_3)_3 \cdot 6H_2O$, $Pr(NO_3)_3 \cdot 6H_2O$, $Nd(NO_3)_3 \cdot 6H_2O$, $Sm(NO_3)_3 \cdot 6H_2O$, $Eu(NO_3)_3 \cdot 6H_2O$, $Gd(NO_3)_3 \cdot 6H_2O$, $Tb(NO_3)_3 \cdot 6H_2O$, $Dy(NO_3)_3 \cdot 5H_2O$, $Ho(NO_3)_3 \cdot 5H_2O$, $Er(NO_3)_3 \cdot 5H_2O$, $Yb(NO_3)_3 \cdot 5H_2O$ were used to prepare the ion solutions. Y, La, and Gd salts were purchased from Chem-Impex International, Inc.; Ce salt from Sigma-Aldrich; Pr, Nd, Sm, Eu, Tb, and Yb salts from Strem Chemicals, Inc.; Dy and Ho salts from Thermo Scientific; and Er salt from Acros Organics. All REE salts were of ≥99% purity. DMF was purchased from Fisher Scientific. All chemicals were used as received without further treatment. The concentration of single REE solutions was 50 mM. For binary REE solutions, the concentration of each cation was 25 mM, and for 13 REE mixture solutions, 5 mM for each cation. All solutions were used at their intrinsic pH values unless otherwise specified. For ion

solutions in DMF or DMF–water mixtures, the hydrated REE salts were first dissolved in DMF and then diluted to the desired ion concentrations and DMF–water molar ratios with deionized (DI) water and DMF.

Preparation of MoS_2-COOH dispersion solution

The aqueous dispersion of single- or few-layer MoS_2 nanosheets was prepared by Li intercalation of bulk MoS_2 powder (Sigma-Aldrich) in *n*-butyllithium solution in hexanes (1.6 M, Sigma-Aldrich), as widely reported previously. The acetic acid functionalization of the exfoliated MoS_2 nanosheets was carried out through nucleophilic substitution reaction with iodoacetic acid (ICH_2COOH, Sigma-Aldrich). Before membrane preparation, the MoS_2-COOH dispersion solution was purified by "washing–filtration–redispersion" cycles, dialysis and centrifugation, according to established procedures by our group.[14] The final dispersion solution was stored under 4 °C for use. Our previous characterization indicated a functionalization degree of approximately 25% –COOH per MoS_2 unit.[24]

Preparation of MoS_2-COOH membrane

The MoS_2-COOH membrane was prepared by vacuum-assisted filtration method. MoS_2-COOH dispersion solution was filtered onto a hydrophilic polytetrafluoroethylene (PTFE) membrane substrate (pore size 0.2 μm; Sigma-Aldrich, Part No. JGWP04700). Following filtration, the MoS_2-COOH/PTFE composite membrane was carefully transferred to clean Petri dishes for natural air drying. To avoid membrane deformation during the drying process, a few drops of DI water were put beneath the membrane to remove air bubbles between PTFE and the dish, ensuring flat and uniform contact. After air drying, the prepared composite membranes were used for ion uptake tests, XRD measurements, and other characterizations.

Membrane uptake test

MoS_2-COOH membranes were soaked into the corresponding REE solutions for at least two days to ensure that ion uptake has reached equilibrium. For dynamic uptake tests, the membranes were soaked for specific time intervals as indicated. Uptake tests of pre-soaked membranes were performed using membranes that had been immersed in the matching solvent at least overnight.

After each uptake test, the membranes were removed from the solutions and thoroughly rinsed (for ~1 min) to remove any ion absorption on the surface. The rinsing was performed using solvent mixtures with the same DMF–water ratio as the corresponding ion solutions. The washed membranes were then dissolved in 3 mL of 3% HNO_3 under sonication overnight. Finally, the leachates were filtered and diluted for ICP-MS analysis.

Attenuated total reflectance Fourier transform infrared (ATR-FTIR) test

MoS_2-COOH membranes were soaked into REE-containing DMF–H_2O mixtures with varying DMF content for at least two days to achieve uptake equilibrium. Prior to measurement, the membrane surface was gently dried with tissue to remove excess solvent while preserving the confined solvent within channels. All spectra were measured using a Shimadzu IRTracer-100 FTIR spectrophotometer

with GladiATR (diamond prism) single bounce ATR attachment. The measurements were collected at wavenumbers from 4000 to 400 cm^{-1} using the following parameters: Happ–Genzel function, 45 scans, and 4 cm^{-1} resolution. The second derivative spectra were determined using the Savitzky–Golay filter.

Author contributions

M. W. and C. L. conceived the project. X. Y. designed the experiments, performed the bulk of the XRD/permeation/uptake tests and analyzed the data. D. Y. contributed to FTIR measurements. X. Y. and C. L. wrote the manuscript. C. L. supervised the project.

Conflicts of interest

The authors declare no conflicts of interest.

Data availability

All data supporting the findings of this study are available within the article and its supplementary information (SI). Supplementary information: additional note, figures, and table. See DOI: https://doi.org/10.1039/d5fd00157a.

Acknowledgements

This work is supported by the Advanced Materials for Energy-Water-Systems (AMEWS) Center, an Energy Frontier Research Center funded by the U.S. Department of Energy, Office of Science, Basic Energy Sciences.

Notes and references

1 B. Radha, A. Esfandiar, F. C. Wang, A. P. Rooney, K. Gopinadhan, A. Keerthi, A. Mishchenko, A. Janardanan, P. Blake, L. Fumagalli, M. Lozada-Hidalgo, S. Garaj, S. J. Haigh, I. V. Grigorieva, H. A. Wu and A. K. Geim, *Nature*, 2016, **538**, 222–225.
2 L. Bocquet, *Nat. Mater.*, 2020, **19**, 254–256.
3 P. Robin and L. Bocquet, *J. Chem. Phys.*, 2023, **158**, 160901.
4 T. Emmerich, N. Ronceray, K. V. Agrawal, S. Garaj, M. Kumar, A. Noy and A. Radenovic, *Nat. Rev. Methods Primers*, 2024, **4**, 69.
5 L. Bocquet and E. Charlaix, *Chem. Soc. Rev.*, 2010, **39**, 1073–1095.
6 J. N. Israelachvili and R. M. Pashley, *Nature*, 1983, **306**, 249–250.
7 C. Y. Lee, J. A. McCammon and P. J. Rossky, *J. Chem. Phys.*, 1984, **80**, 4448–4455.
8 G. Cicero, J. C. Grossman, E. Schwegler, F. Gygi and G. Galli, *J. Am. Chem. Soc.*, 2008, **130**, 1871–1878.
9 M. F. Toney, J. N. Howard, J. Richer, G. L. Borges, J. G. Gordon, O. R. Melroy, D. G. Wiesler, D. Yee and L. B. Sorensen, *Nature*, 1994, **368**, 444–446.
10 L. Fumagalli, A. Esfandiar, R. Fabregas, S. Hu, P. Ares, A. Janardanan, Q. Yang, B. Radha, T. Taniguchi, K. Watanabe, G. Gomila, K. S. Novoselov and A. K. Geim, *Science*, 2018, **360**, 1339–1342.

11 R. Wang, M. Souilamas, A. Esfandiar, R. Fabregas, S. Benaglia, H. Nevison-Andrews, Q. Yang, J. Normansell, P. Ares, G. Ferrari, A. Principi, A. K. Geim and L. Fumagalli, *Nature*, 2025, **646**, 606–610.
12 N. Kavokine, S. Marbach, A. Siria and L. Bocquet, *Nat. Nanotechnol.*, 2019, **14**, 573–578.
13 D. Toquer, L. Bocquet and P. Robin, *J. Chem. Phys.*, 2025, **162**, 064703.
14 M. Wang, T. Sadhukhan, N. H. C. Lewis, M. Wang, X. He, G. Yan, D. Ying, E. Hoenig, Y. Han, G. Peng, O.-S. Lee, F. Shi, D. M. Tiede, H. Zhou, A. Tokmakoff, G. C. Schatz and C. Liu, *Proc. Natl. Acad. Sci. U. S. A.*, 2024, **121**, e2313616121.
15 M. Wang, Q. Xiong, X. Yue, G. Yan, Y. Han, Z. Lyu, Z. Li, L. Sun, E. Hoenig, K. Xu, N. H. C. Lewis, K. M. Merz, Q. Chen, G. C. Schatz and C. Liu, *Nat. Commun.*, 2025, **16**, 5854.
16 Z. Yu, P. E. Rudnicki, Z. Zhang, Z. Huang, H. Celik, S. T. Oyakhire, Y. Chen, X. Kong, S. C. Kim, X. Xiao, H. Wang, Y. Zheng, G. A. Kamat, M. S. Kim, S. F. Bent, J. Qin, Y. Cui and Z. Bao, *Nat. Energy*, 2022, **7**, 94–106.
17 J. Xu, J. Zhang, T. P. Pollard, Q. Li, S. Tan, S. Hou, H. Wan, F. Chen, H. He, E. Hu, K. Xu, X.-Q. Yang, O. Borodin and C. Wang, *Nature*, 2023, **614**, 694–700.
18 J. Self, K. D. Fong and K. A. Persson, *ACS Energy Lett.*, 2019, **4**, 2843–2849.
19 D. Lu, R. Li, M. M. Rahman, P. Yu, L. Lv, S. Yang, Y. Huang, C. Sun, S. Zhang, H. Zhang, J. Zhang, X. Xiao, T. Deng, L. Fan, L. Chen, J. Wang, E. Hu, C. Wang and X. Fan, *Nature*, 2024, **627**, 101–107.
20 J. Smiatek, A. Heuer and M. Winter, *Batteries*, 2018, **4**, 62.
21 R. A. Miranda-Quintana and J. Smiatek, *J. Phys. Chem. B*, 2021, **125**, 13840–13849.
22 S. Liao, Y. Liu, L. Li, L. Ding, Y. Wei and H. Wang, *Nat. Commun.*, 2025, **16**, 6675.
23 X. Chen, Y. Qin, Y. Zhu, X. Pan, Y. Wang, H. Ma, R. Wang, C. D. Easton, Y. Chen, C. Tang, A. Du, A. Huang, Z. Xie, X. Zhang, G. P. Simon, M. M. Banaszak Holl, X. Lu, K. Novoselov and H. Wang, *Sci. Adv.*, 2024, **10**, eadl1455.
24 E. Hoenig, S. E. Strong, M. Wang, J. M. Radhakrishnan, N. J. Zaluzec, J. L. Skinner and C. Liu, *Nano Lett.*, 2020, **20**, 7844–7851.
25 L. Huang, Y. Li, Q. Zhou, W. Yuan and G. Shi, *Adv. Mater.*, 2015, **27**, 3797–3802.
26 A. E. Yaroshchuk, *Adv. Colloid Interface Sci.*, 2000, **85**, 193–230.
27 R. Epsztein, R. M. DuChanois, C. L. Ritt, A. Noy and M. Elimelech, *Nat. Nanotechnol.*, 2020, **15**, 426–436.
28 T. Cheisson and E. J. Schelter, *Science*, 2019, **363**, 489–493.
29 K. Das, K. Bose and K. K. Kundu, *Electrochim. Acta*, 1981, **26**, 479–485.
30 H. Kobara, A. Wakisaka, K. Takeuchi and T. Ibusuki, *J. Phys. Chem. B*, 2003, **107**, 11827–11829.
31 A. C. Kumbharkhane, S. M. Puranik and S. C. Mehrotra, *J. Solution Chem.*, 1993, **22**, 219–229.
32 G. Papanastasiou and I. Ziogas, *Anal. Chim. Acta*, 1989, **221**, 295–303.
33 L. P. Hammett, *Physical Organic Chemistry*, McGraw-Hill Company, New York City, 1940.
34 E. Buncel and E. A. Symons, *Can. J. Chem.*, 1970, **48**, 3354.
35 M. H. Motevaselian and N. R. Aluru, *ACS Nano*, 2020, **14**, 12761–12770.

36 M. Wang, Q. Xiong, M. Wang, N. H. C. Lewis, D. Ying, G. Yan, E. Hoenig, Y. Han, O.-S. Lee, G. Peng, H. Zhou, G. C. Schatz and C. Liu, *Sci. Adv.*, 2024, **10**, eadh1330.

